









Open Archive Toulouse Archive Ouverte (OATAO)

OATAO is an open access repository that collects the work of Toulouse researchers and makes it freely available over the web where possible

This is a Publisher's version published in: <http://oatao.univ-toulouse.fr/24651>

Official URL: <https://doi.org/10.1016/B978-0-12-817744-0.00003-9>

To cite this version:

Manière, Charles  and Kus, Ugras  and Chevallier, Geoffroy  and Weibel, Alicia  and Durand, Lise and Huez, Julitte  and Delagnes, Denis and Estournès, Claude  *How to overcome the main challenges of SPS technology: Reproducibility, multi-samples and elaboration of complex shapes.* (2019) In: Spark Plasma Sintering. UNSPECIFIED, 77-108. ISBN 978-0-12-817744-0

Any correspondence concerning this service should be sent to the repository administrator: tech-oatao@listes-diff.inp-toulouse.fr

CHAPTER 3

How to overcome the main challenges of SPS technology: Reproducibility, multi-samples and elaboration of complex shapes

C. Manière^{*,†}, U. Kus^{*,‡}, G. Chevallier^{*}, A. Weibel^{*}, L. Durand[†],
J. Huez[‡], D. Delagnes[§], C. Estournès^{*}

^{*}CIRIMAT, Université de Toulouse; CIRIMAT, CNRS, Université Toulouse III—Paul Sabatier, Toulouse, France

[†]CEMES, CNRS UPR 8011 and University of Toulouse, Toulouse, France

[‡]CIRIMAT, University of Toulouse, CNRS, INP-ENSIACET, Toulouse, France

[§]Clément Ader Institute (ICA), University of Toulouse, CNRS, Mines Albi, INSA, UPS, ISAE-SUPAERO, Toulouse, France

1. Introduction

The spark plasma sintering process (SPS) permits the densification of a wide variety of materials [1–2] (metals, alloys, ceramics, polymers, and composites). This breakthrough sintering technique is able to create highly dense materials with micro-structural control and a very short processing time [3–5]. Although it has experienced a very strong growth in the last three decades in terms of publications and patents, its industrialization is still in its infancy. This is mainly due to the fact that pieces of simple geometries have been densified so far, and that this technology is considered to suffer from a lack of reproducibility and productivity. We will try to show in this chapter, how to overcome three of the main challenges of SPS technology: reproducibility, multi-samples, and elaboration of complex shapes.

2. Reproducibility

Phenomenon occurring during Spark-Plasma-Sintering (SPS) still need more investigation to fully control the process. The control of the sintered material requires more understanding, particularly on the phenomena leading to a lack of reproducibility. Dog-bone shaped samples of the Ti-6Al-4V alloy have been sintered to full density to validate whether SPS offers the

possibility to obtain repeatable complex pieces or not. The material was chosen due to its microstructure—highly dependent on temperature—which could easily reflect gradients in the densified samples. Tensile properties were evaluated to compare their values (i.e., reproducibility) and whether the SPS samples exhibit the same level of performance as annealed and solution-treated forged alloy.

2.1 Introduction

Titanium alloys are of great interest, especially for aerospace and biomedical applications because of their biocompatibility and their high specific mechanical and corrosion properties [6]. Large-scale production is still restricted because of the high cost and the technical complexity of titanium extraction. Furthermore, thermomechanical treatment applied on raw materials is also a huge part of the final product cost. This is directly related to the final shape complexity. It is therefore essential to use titanium alloys in the most efficient way to minimize the amount of wasted material. Near Net Shape (NNS) processing offers the possibility to meet this need and to simplify processes by reducing the number of steps. Powder metallurgy is one of the methods of NNS fabrication used for the Ti-6Al-4V [7–14] and this work specifically concerns the use of Spark Plasma Sintering (SPS). In this process, the heat is created by a pulsed electric current passing through the die and the powder. It allows high heating rates (up to 1000°C/min) and shorter sintering duration. This is, as claimed by its inventor, is due to the presence of sparks between granules which lead to the cleaning of their surfaces and to the generation of plasma which facilitates the diffusion process [15–17]. Other effects, like the rapid activation of plastic deformation at the contact points of the granules, are still being discussed in the literature [18]. These phenomena enhance mass transport at these points and contribute to obtain shorter sintering duration. It is a well-known phenomenon in SPS of conductive powders that the temperature inside the powder is higher than the set point temperature [15,18–21]. Therefore, powder temperature is higher than the die temperature. For all these reasons, homogeneity and control of the temperature inside the powder, i.e., control of the microstructure and the mechanical properties of the sintered sample, can be difficult, and needs more investigation.

The aim of this work is to evaluate repeatability of the SPS process in terms of density, microstructures, and mechanical properties of the samples elaborated. In order to achieve this target, 12 NNS samples (complex shapes)

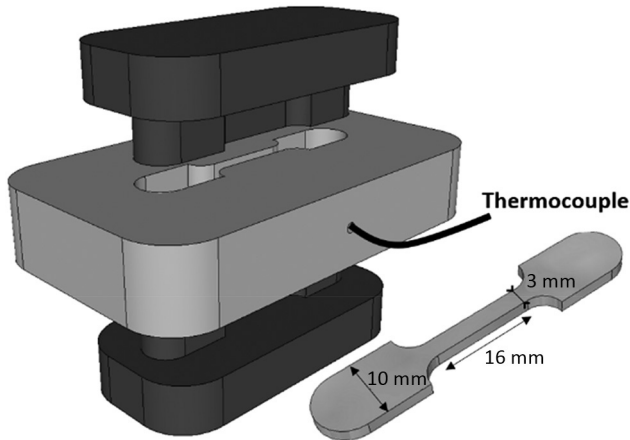


Fig. 1 Scheme of the stack and the produced samples.

have been sintered in the same conditions using specific dies already tested [22] (Fig. 1). Gauge-length microstructures of all the samples are observed using optical microscopy (OM) and tensile properties are characterized. Mechanical behavior of these specimens is a point of interest in order to evaluate this technique with regard to the already used process for aeronautical applications.

2.2 Materials and procedure

2.2.1 As received material

A pre-alloyed powder of Ti-6Al-4V provided by the French company Aubert & Duval [23] has been used. It was produced by Plasma Rotating Electrode Process (PREP) [24] and its chemical composition is detailed in Table 1.

It results in the formation of spherical and full granules (Fig. 2A) which are benefits to full densification of the material by sintering [6]. The Beta transus (T_{β}) has been measured by differential thermal analysis (using a Setaram Setsys 16/18) and a value about 991°C has been obtained. The granule diameter distribution is from 40 to 400 μm (Fig. 2B). The average

Table 1 Chemical composition of the ARP (obtained by inductively coupled plasma and combustion methods)

Element	Al	V	Fe	C	N	O	Ti
[%wt.]	6.12	4.06	0.19	0.014	0.003	0.15	base

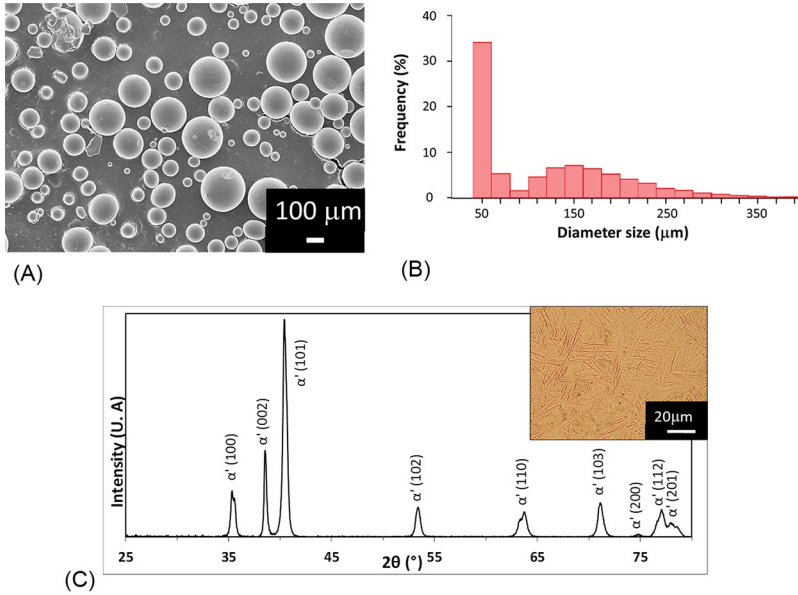


Fig. 2 (A) SEM micrography, (B) size distribution, and (C) X-ray diffraction of the TA6V powder.

ex-β-grain size could only be determined on the granules above 100 μm of diameter and is about 55 μm. X-ray diffraction (using a BRUKER D8 ADVANCE) and OM (using a NIKON Eclipse MA200) reveal that the microstructure of the ARP is martensitic, due to high speed cooling during PREP (Fig. 2C).

2.2.2 Spark plasma sintering (SPS)

A Dr. Sinter 2080 unit (from SPS Syntex Inc., Japan) of the Plateforme Nationale de Frittage Flash located at Université Toulouse III Paul Sabatier, Toulouse, France was used to densify the samples. The powder was introduced into an NNS die made of WC-Co (6.5%wt) and specific punches in graphite were used (Fig. 1). This system produces a ready-to-test sample. For easy removal, a graphitic sheet was placed between each punch and the powder, and a graphitic spray was used between the die and the powder. Sintering was performed in vacuum (residual cell pressure <10 Pa). A thermocouple, inserted in a hole, 3 mm in depth, at the surface of the die, was used to monitor the temperature up to the set point.

The sintering cycle is described as follows: a precompaction was completed at room temperature at about 25 MPa and released, to have the same

initial green compaction of the powder for all samples. Heating rates of 50°C/min from room temperature to 500°C, then 25°C/min up to the dwell temperature of 800°C, were used. This temperature had been chosen because temperature gradients are present in the sintering system [15,18–21]. In fact, previous work revealed that this temperature leads to a temperature close to T_{β} in the gauge length of the future sample during sintering [25]. As the aim of this work was to evaluate the repeatability, this temperature field was particularly interesting. The dwell time was 20 min. This time had been chosen to characterize the system at thermal-stability conditions. A pressure of 100 MPa was applied within the first minute at the dwell and maintained during it. Both pressure and temperature were released suddenly at the end of the dwell (the load within 1 min; the temperature within 30 min by free cooling). The vacuum was maintained during natural cooling until 300°C. The stack (die containing the sample and punches) was then removed from the SPS unit and air-cooled.

In order to remove the potential surface pollution due to graphite spray from the samples and to improve the roughness, 400 μm was removed from top, bottom, and lateral surfaces of the gauge length by resurfacing (this is done after the thermal treatment applied for five samples). A scheme of the as-ready-to-test samples is presented in Fig. 1. Twelve samples were prepared with the same conditions and named in the following NNS01 to NNS12, respectively.

The density of all the samples has been determined using Archimedes' method and the Relative Density (RD) has been calculated taking into consideration a theoretical value of 4.43 g/cm³. The RD values of all the sintered samples are reported in Table 2.

Electric dissipated power is calculated from tension and intensity data recorded by the sinter unit to compare temperature reached by the powder for the same sintering conditions between all the sintering cycles.

2.3 Results and discussion

Sintering parameters of some of the sintered samples are reported in Fig. 3. Calculated electric dissipated power (EDP) curves are also plotted (in black). The curve of NNS04 is representative for the samples NNS04 to NNS12. All the samples have relative densities higher than 99.5%. As the observations of the microstructures do not reveal any porosity, one can assume that all the samples are fully dense.

Table 2 Samples densities and maximum electric dissipated power

Sample	NNS01	NNS02	NNS03	NNS04	NNS05	NNS06	NNS07	NNS08	NNS09	NNS10	NNS11	NNS12
RD ($\pm 0.5\%$)	99.6	99.5	99.8	99.7	99.7	99.6	99.6	99.6	99.6	99.7	99.7	99.6
Max.EDP(W)	6180	6860	5730	5760	5690	5800	5560	5410	5690	5730	5600	5500

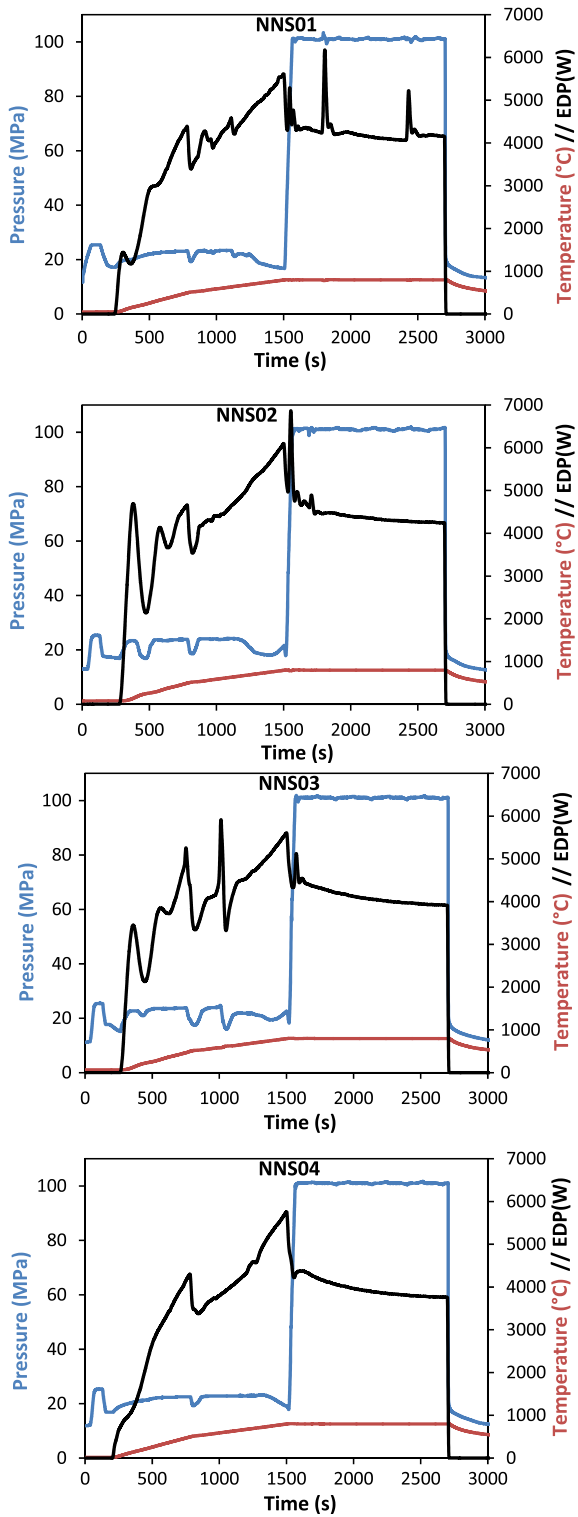


Fig. 3 Representative sintering cycles for all the samples.

Maximum EDP reported in Table 2 are very similar for all the samples (5647 ± 125 W) from NNS03 to NNS12, while for NNS01 and NNS02 the values are higher (>6100 W). Although some peaks are observable on the NNS03 EDP curve during heating, the maximum EDP is close to the average value of samples NNS04 to NNS12. This should have no impact on microstructure.

The microstructures of the gauge lengths of four samples are presented in Fig. 4. Some differences are also discernable in the two families of samples. NNS01 has a microstructure where over transus temperature (T_{β}) treated areas (presence of lamellar structure) are observed. As has been mentioned before, our previous work revealed that, because of the presence of a temperature gradient, a set point temperature of 800°C in this system leads to a temperature of the gauge length close to T_{β} [15,18–21]. Previous work revealed that such types of areas exist when the temperature of the sample has reached around 975°C [26]. NNS02 has a through T_{β} processed microstructure (necklace microstructure) [6] that is observed in all gauge lengths.

RD and maximum EDP reported on the graph of all the samples sintered in this work are detailed in Table 2.

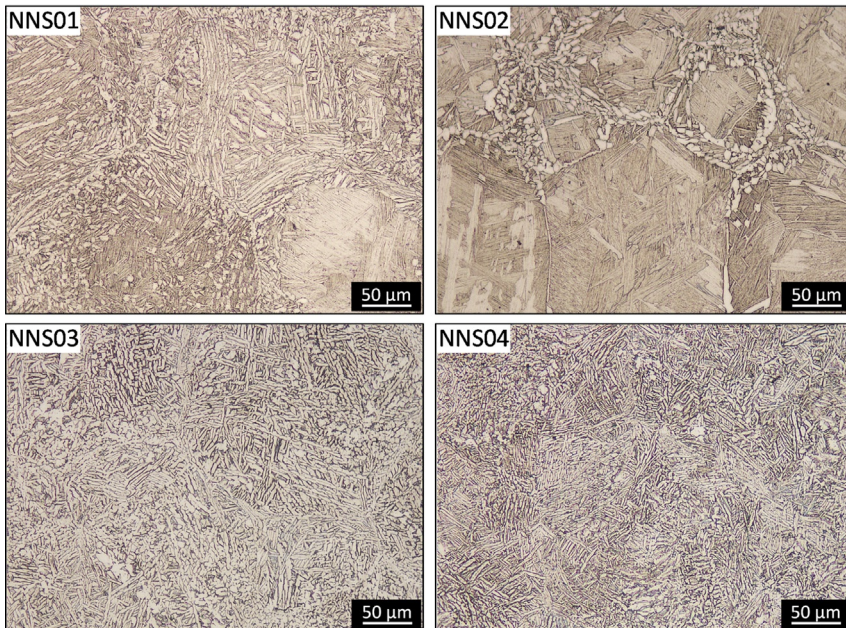


Fig. 4 Microstructures of the NNS specimens observed at Optical Microscopy.

This leads us to conclude that the temperature in the powder during the sintering was higher than the temperature of NNS01. Such types of microstructure can be explained by the temperature of the sample during the sintering being close to, but higher than, the transus. This high temperature can be explained by an EDP_{max} higher than the one of the sample NNS01. Here, we can assume that EDP_{max} is a good indicator of the temperature reached during the sintering, at least comparatively. NNS03 and NNS04 have microstructures composed of equiaxed alpha grains and lamellae from aged martensite. Microstructures of NNS03 and NNS04 are completely treated in the $\alpha + \beta$ field. They are close and are representative of the other samples (Number > NNS04). Thanks to in-situ temperature measurement, we can assume that the temperature of the powder is between 920°C and 975°C during the sintering.

Observations of the stack during SPS let us identify the reasons for these discrepancies on the EDP_{max} and the obtained microstructures. A nonsymmetric position of the punch on the up side and the down side of the die led to difficulties controlling the current in the stack. This is due to different vertical surfaces between the top punch/die and the bottom punch/die (Fig. 5). This dissymmetry may induce different local electrical contact resistances [27,28], leading to EDP peaks for NNS01 and NNS02. Vertical surface differences between top punch/die and bottom punch/die are lower for NNS03 and the maximum EDP is close to other samples.

The correlation observed between the microstructure and the EDP Max values seems to indicate this latter parameter is correct to estimate the higher temperature reached by a sample for the same sintering conditions.

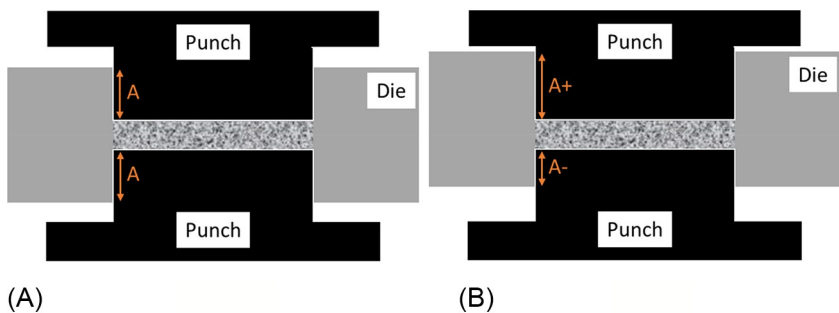


Fig. 5 Cross-section of the SPS Tool: (a) symmetric position of the punches with regard to the powder/die; (b) asymmetric position of the punches (top one more pushed than the bottom one inside the die).

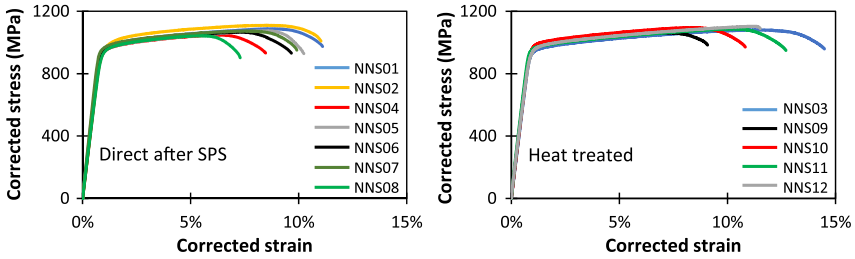


Fig. 6 Tensile test curves of sample recorded after thermal treatment.

Before characterization of tensile properties, five samples are annealed at 730°C for 2h in order to remove potential residual stress due to plastic deformation during sintering or cooling. The curves of tensile tests for each type of specimen are plotted in Fig. 6. Average Young modulus (E), yield strength at 0.2% (σ_y) and ultimate tensile strength (UTS) of each type of specimen are reported in Table 3.

Failure strains are different between the two types of specimen (directly after SPS and heat treatment). After heat treatment, the strain is improved by about 2%. This indicates that there is some residual stress in the NNS specimens after the SPS. Nevertheless, no significant softening can be observed. For each kind of specimen, properties are quite similar, which proves good repeatability on mechanical properties. Furthermore, discrepancies observed on microstructures do not have any significant impact on mechanical properties. Comparison to other processes is not the aim of this work and will be more detailed in future publications. However, some trends are described. σ_y and UTS measured in this paper are of the same level or higher than properties obtained on SPSed samples [7]. Properties are higher than casting and hot isostatic pressing (HIP) [10,14,29–31] but the failure strain is lower than HIP (due to slower cooling after HIP). Tensile properties reported in this paper are of the same level as annealed forged alloy [31,32] and of the same as the lower level of solution treated forged alloy [31–33] but the properties of specimen presented in this paper could be improved by solution thermal treatment after SPS.

Table 3 Tensile properties of all the sintered specimens

Sample type	E (GPa)	σ_y (MPa)	UTS (MPa)	Failure strain
Direct	116 ± 4	949 ± 6	1073 ± 21	$9.8 \pm 1.3\%$
After heat treatment	113 ± 4	970 ± 12	1085 ± 18	$11.7 \pm 2.3\%$

2.4 Conclusions

NNS specimens have been successfully sintered by SPS. All densities have been measured above 99.6% and microstructural observations reveal no porosity. It is then assumed that NNS specimens are completely dense. Analyses of the sintering parameters and microstructure characterization realized in this paper reveal that ten specimens out of twelve are identical. The other two have some differences on sintering cycles and microstructures. Anyway, reasons that led to these discrepancies are identified (nonsymmetric positioning of the punches). Therefore, it has been demonstrated that it is possible to obtain strictly identical sintering parameters and microstructures. Furthermore, all measured tensile properties are similar. SPS is then a process able to produce completely dense NNS specimens with very similar microstructures and tensile properties, at the same level as annealed and solution treated forged alloy.

3. Multi samples

3.1 Introduction

The SPS process has the potential for the densification of a wide variety of materials with an interesting capacity to control the microstructure. Thanks to these benefits, this technology is increasingly used globally for research field. Unlike its country of origin, the industrialization of this technology is lagging behind in Europe. One of the main reasons for this is its low productivity. Indeed, in most of the published work about the SPS process, the technology is presented in its classical configuration where only one sample is produced per cycle. Despite this observation, several solutions exist to reconcile productivity and advanced materials properties. The first approach consists of minimizing the time duration of each cycle. A reduction of the cycle duration to a few seconds is possible using a pressure-assisted welding machine for electrically conductive materials [34] or a process close to flash sintering [35] performed in the SPS machine [36]. It is also possible to save significant processing time by an optimization of the manufacturing steps. For example, fully automated tunnel [37] or rotational-type [38] production chains exist to optimize the vacuum, load, and preheating steps [3].

The other approach consists of sintering simultaneously a high number of samples. As explained in the review of Guillon et al. [4], it is possible to sinter simultaneously several samples by parallel [39–41], serial, or serial/parallel multi-parts configurations. This solution is of greater interest considering

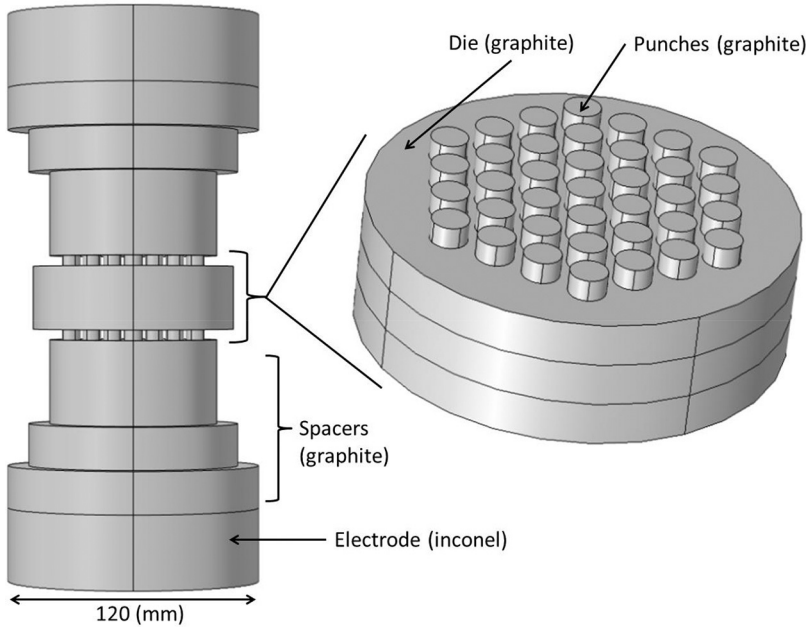


Fig. 7 37 samples parallel configuration.

the short processing time of the SPS (a few minutes) compared to the other sintering techniques such as conventional sintering or hot pressing (hours or days).

The possibility to sinter simultaneously a high quantity of samples is studied in this part of the paper. A first parallel disposition of 37 samples (Fig. 7) is studied experimentally, and simulated by an FEM electro-thermal-mechanical-microstructural model. Further, a parallel/serial configuration with 111 samples (Fig. 8) has been studied by the simulation approach only, as the column height of our machine does not allow us to test this configuration experimentally. For both configurations, a temperature difference between the die center and edge is observed and is responsible for a grain size difference, while the samples' densification homogeneity appears to be correct. An optimization of the temperature homogeneity performed by simulation and presented later in this chapter evidences that homogenization of the radial temperature in the parallel samples configuration is made possible by the introduction of electric insulating layers in the central samples. For the parallel/serial configurations, an external die can be used to homogenize the temperatures.

One of the main problems of the SPS of complex shapes or high dimension tools is temperature nonhomogeneity. Electro-thermal modeling (ET)

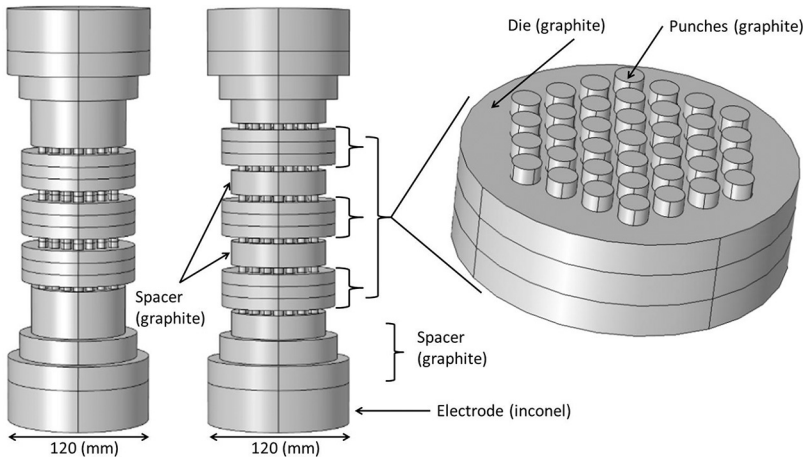


Fig. 8 Serial parallel multiple parts configurations with or without intermediate spacer.

is then of a great interest, as it allows us to predict and find solutions to correct the thermal gradients [19,42]. For this purpose, more or less complex Joule heating models are employed [43–47]. The first models were very simple and point out the high production of heat at the level of the punches and the main differences in temperature distribution between electrically insulating and conductive samples [48,49]. More complex ET models appear today and highlight the great importance of the electrical and thermal contact resistances (ECR and TCR) in all the column inner interfaces [19,50–52]. These ECR and TCR depend on many factors, such as the interface temperature and pressure. They are difficult to determine because an SPS experiment represents a very large experimental domain of internal temperature and pressure. For this reason, an increasing number of authors chose to determine them by in-situ measurements [53,54] or calibration [21,22,27,55]. In our previous study, we used a calibration methodology to determine the ECR and TCR of the SPS column based on temperature measurement with thermocouples placed at different strategic points. The same approach is used in this work to determine the relevant ECR and TCR of our configuration.

For the sintering part, the Olevsky's mechanical–microstructural (MM) model [56,57] is employed to simulate both the powder densification and the grain growth. In previous papers, we determined the densification parameters [58], the behavior of the grain growth [59], and the powder/die friction [60] of the alumina powder used in this paper.

3.2 Materials and SPS densification

All the experiments were performed on the SPS machine (Dr. Sinter 2080, SPS Syntex Inc., Japan) of the Plateforme Nationale CNRS de Frittage Flash located at the Université Toulouse III-Paul Sabatier in Toulouse. In the parallel multiple parts densification of the 37 samples configuration (Fig. 7), 1 g of powder (alumina 99.99%, reference TM-DAR, Taimei Chemicals Co. Ltd) is loaded inside each of the cylindrical holes of 8 mm diameter. The electrodes are in Inconel, the other tools are in 2333 graphite [61]. A graphite foil called “papyex” [62] is introduced at the vicinity of the interface in contact with the powder and two foils are introduced at the electrode/spacer interfaces. The vertical die face is covered with a graphite felt [63] and an optic pyrometer is employed for die wall temperature control (a hole is created in the graphite felt to allow die temperature measurement). The thermal cycle of the Fig. 7 experiment is a 15 min dwell at 600°C to allow the stabilization of temperature detection (from 575°C), then a 100°C/min temperature ramp up to 1300°C and a 5 min dwell is performed. The pressure cycle is 3 MPa for the first 19 min and a 1 min ramp up to 11 MPa; this pressure is maintained for the rest of the cycle. We were very cautious with the applied pressure for this test because we wanted to avoid any problems of die failure.

The ECR, TCR calibration test is performed in the configuration reported in Fig. 9A. This configuration is very close to the parallel 37 samples

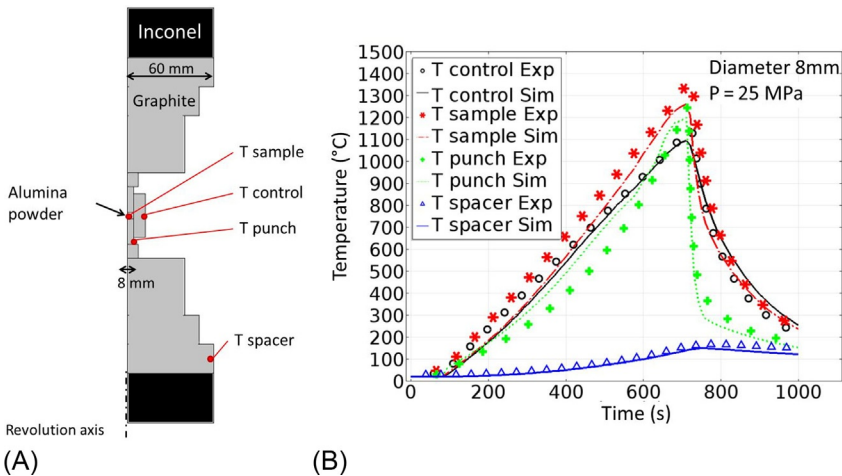


Fig. 9 ECR and TCR calibration: (A) experimental geometry and thermocouples positions (B) experimental/modeled temperatures after calibration.

configuration of Fig. 7 except there is only one sample. To calibrate the ECR and TCR with the method describe in [22,27], four K type thermocouples are placed in the powder, the die, the punch, and the lower spacer. A Rogowski coil sensor is employed to measure the RMS current used as input electric condition for the Joule heating model. The temperature and pressure cycles need to be in the most useful possible domain for multiple parts experiments. After the success of our test at 11 MPa, we chose to perform our calibration experiment and the simulations at 25 MPa (from the start). The calibration test thermal cycle is a simple 100°C/min temperature ramp up to 1100°C.

Field-emission-gun scanning electron microscopy (FEG-SEM, JEOL JSM 6700F) observations on fractured samples were performed at the TEMSCAN facility, Université Toulouse III Paul-Sabatier.

3.3 Finite element model

The paragraphs below are devoted to the description of the ETMM model and the materials properties.

3.3.1 The electro-thermal-mechanical-microstructural model

The ETMM model is a fully coupled model of a Joule heating part (ET) and a sintering part (MM). The sintering part includes a grain growth model coupled with a densification model.

3.3.1.1 The electro-thermal model

The Joule heating model is built up with two main equations: the equation of electrical charge conservation (1) and the heat Eq. (2).

$$\nabla \cdot \vec{J} = \nabla \cdot (\sigma \vec{E}) = \nabla \cdot (-\sigma \nabla U) = 0 \quad (1)$$

$$\nabla \cdot (-\lambda \nabla T) + \rho C_p \frac{\partial T}{\partial t} = \vec{J} \cdot \vec{E} \quad (2)$$

where

J is the current density;

U is the electric potential;

E is the electric field;

T is the absolute temperature and for each of the materials of the device;

λ is the thermal conductivity;

σ is the electric conductivity;

ρ is the density; and

C_p is the calorific capacity.

Two main thermal limit conditions are employed to model the radiative flux (3) on the vertical walls and the conducto-convective flux (4) on boundary limits near the water cooling system.

$$\phi_r = \sigma_s \cdot \epsilon \cdot (T_e^4 - T_a^4) \quad (3)$$

where

- ϕ_r is the radiative heat flux;
- σ_s is the Stefan-Boltzmann's constant;
- T_e is the emission surface temperature;
- ϵ is the emissivity; and
- T_a is the chamber wall temperature.

$$\phi_c = h_c \cdot (T_i - T_w) \quad (4)$$

where

- ϕ_c is the conducto-convective heat flux;
- T_i is the wall surface temperature, T_w the water temperature; and
- h_c is the conducto-convective coefficient.

The electric and thermal contact resistances present at the different inner interfaces between the parts obey:

$$J_c = \sigma_c (U_1 - U_2) \quad (5)$$

$$\dot{q}_c = h_{cr} (T_1 - T_2) \quad (6)$$

where

- J_c and \dot{q}_c are the current density and the heat flux across the contact, respectively;
- U_i and, T_i the electric potential and temperature on each side of the contact interface, respectively,
- σ_c is the electric contact conductance; and
- h_{cr} is the thermal contact conductance.

3.3.1.2 The mechanical-microstructural model

Olevsky's model of sintering is based on a creep power law.

$$\sigma(W) = KW^m \quad (7)$$

where

- $\sigma(W)$ is the equivalent stress;
- W is the equivalent strain rate; and
- K is the consistency factor.

Following Olevsky's work [57] and our previous work [58], the temperature and grain size dependence of K is:

$$K = \left(\frac{G}{G_0} \right)^2 \frac{1}{A_0^m} T^m \exp\left(\frac{mQ}{RT} \right) \quad (8)$$

where

G is the average grain diameter;

G_0 is the initial grain size;

A_0 is a constant;

T is the absolute temperature;

R is the gas constant;

m is the strain rate sensibility exponent; and

Q is the power law creep activation energy.

The power law creep equivalent strain rate of porous solids W is:

$$W = \frac{1}{\sqrt{1-\theta}} \sqrt{\varphi\dot{\gamma}^2 + \psi\dot{\epsilon}^2} \quad (9)$$

where φ and ψ are two functions of the porosity θ , the normalized shear modulus and the normalized bulk modulus, respectively. These functions are [56]:

$$\varphi = (1-\theta)^2 \quad (10)$$

$$\psi = \frac{2(1-\theta)^3}{3\theta} \quad (11)$$

The shrinkage rate $\dot{\gamma}$ and shape rate change $\dot{\epsilon}$ are invariant of the strain rate tensor $\dot{\epsilon}$:

$$\dot{\gamma} = \sqrt{2\left(\dot{\epsilon}_{xy}^2 + \dot{\epsilon}_{xz}^2 + \dot{\epsilon}_{yz}^2\right) + \frac{2}{3}\left(\dot{\epsilon}_x^2 + \dot{\epsilon}_y^2 + \dot{\epsilon}_z^2\right) - \frac{2}{3}\left(\dot{\epsilon}_x\dot{\epsilon}_y + \dot{\epsilon}_x\dot{\epsilon}_z + \dot{\epsilon}_y\dot{\epsilon}_z\right)} \quad (12)$$

$$\dot{\epsilon} = \dot{\epsilon}_x + \dot{\epsilon}_y + \dot{\epsilon}_z \quad (13)$$

The stress tensor σ for a porous body is then:

$$\underline{\sigma} = \frac{\sigma(W)}{W} \left(\varphi \underline{\dot{\epsilon}} + \left(\psi - \frac{1}{3}\varphi \right) \dot{\epsilon} i \right) \quad (14)$$

The mass conservation equation is employed to determine locally the porosity θ :

$$\frac{\dot{\theta}}{1-\theta} = \dot{\epsilon}_x + \dot{\epsilon}_y + \dot{\epsilon}_z \quad (15)$$

The grain growth expression [57] is:

$$\dot{G} = \frac{k_0}{3G^2} \left(\frac{\theta_c}{\theta_c + \theta} \right)^{\frac{3}{2}} \exp \left(\frac{-Q_G}{RT} \right) \quad (16)$$

where

\dot{G} is the grain growth rate;

k_0 is a constant;

θ_c is a critical porosity; and

Q_G is the activation energy of the grain growth.

In a viscous-plastic approach it is possible to describe the powder/die friction using the expression of the tangential stress (17) determined in a previous work [60]. However, we chose to neglect this phenomenon because, in the same work, we discovered that the powder/die friction can be neglected with an alumina powder and if we use a graphite foil at the interface.

$$\tau = -\mu K \frac{1}{2} \frac{\varphi^{\frac{m+1}{2}}}{(2(1-\theta))^{\frac{m-1}{2}}} |V_g|^{m-1} V_g \quad (17)$$

where

τ is the friction tangential stress;

μ is the friction coefficient; and

V_g is the relative velocity of the sliding interface.

3.3.2 Materials properties

The ETMM simulation requires many parameters for each of the corresponding physics. All the sintering (MM) parameters of alumina were determined in our previous study [58] on the same alumina powder. Concerning the Joule heating part (ET), the material properties of the tools are given in our previous work [27] and derived from the manufacturer's measurements [61–63]. Only the ECR and TCR of all the inner interfaces are missing and are determined by calibration. The general table of all our ETMM parameters is reported in Table 4.

3.4 Results and discussions

3.4.1 Experimental results for the parallel configuration

In order to differentiate each of the 37 samples of the parallel experiment (Fig. 7), an XY coordinate system is employed (Fig. 10A). All the 37 samples after demolding are reported in Fig. 10B. The four samples of the X-axis radius (00, 01, 02, and 03) are characterized to study the differences between

Table 4 ETMM model parameters [27,57,58]

ET properties	Inconel	Graphite	Alumina
Heat capacity C_p ($\text{J kg}^{-1} \text{K}^{-1}$)	$344 + 2.50 \times 10^{-1} T$	$34.27 + 2.72 T - 9.60 \times 10^{-4} T^2$	$850 (1 - \theta)$
Thermal conductivity λ ($\text{W m}^{-1} \text{K}^{-1}$)	$10.1 + 1.57 \times 10^{-2} T$	$123 - 6.99 \times 10^{-2} T + 1.55 \times 10^{-5} T^2$	$39,500 T^{-1.26} (1 - 3\theta/2)$
Electrical resistivity ρ_e (Ωm)	$9.82 \times 10^{-7} + 1.6 \times 10^{-10} T$	$1.70 \times 10^{-5} - 1.87 \times 10^{-8} T$ $+ 1.26 \times 10^{-11} T^2 - 2.44 \times 10^{-15} T^3$	$8.70 \times 10^{19} T^{-4.82} (1 - 3\theta/2)^{-1}$
Density ρ (kg m^{-3})	8430	$1904 - 0.01414 T$	$3899 (1 - \theta)$
MM properties	Alumina		
Creep parameter m	1		
Creep parameter A_0 ($\text{s}^{-1} \text{KPa}^{-n}$)	0.873		
Creep parameter Q (kJ/mol)	179		
Creep parameter G_0 (μm)	0.14		
Grain growth parameter k_0 (m^3/s)	7×10^{-4}		
Grain growth parameter θ_c	0.05		
Grain growth parameter Q_G (kJ/mol)	520		

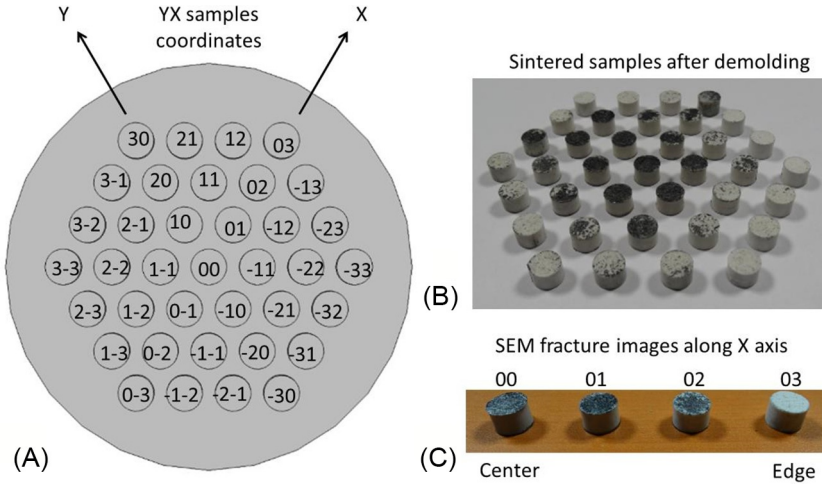


Fig. 10 (A) Samples location and coordinate, (B) sintered samples, (C) the four samples used for the analysis.

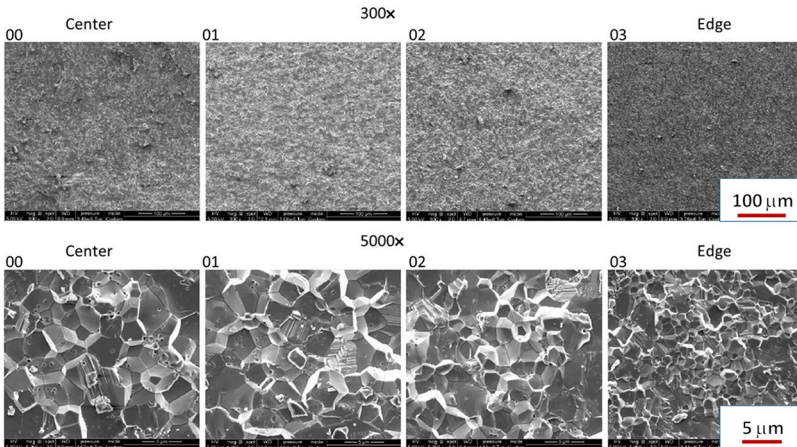


Fig. 11 SEM images of the four samples from the center to the edge of the die at a magnification of 300 × and 5000 ×.

the center and the edge of the die (Fig. 10C). The relative densities are determined by Archimedes' method. To determine the average grain size, the Mendelson [64] method is used from the samples fracture images reported in Fig. 11. The relative densities and average grain sizes are reported in Table 5.

Table 5 Relative density and average grain size of the X-axis samples from the center to the edge

Samples (X axis)	00	01	02	03
Relative density	0.97 ± 0.01	0.989 ± 0.001	0.988 ± 0.001	0.975 ± 0.001
Average grain size (μm)	6.59 ± 0.05	6.40 ± 0.05	5.85 ± 0.05	3.45 ± 0.05

The fracture images show dense samples of about 97%, and average grain size close to $6\mu\text{m}$ for the sample at the center, and $3.45\mu\text{m}$ for the edge sample. This result suggests the presence of a thermal gradient between the center sample (hot) and the edge (cooler).

This first test in the simplest configuration demonstrates the possibility to sinter simultaneously a high number of samples with acceptable difference in microstructure. This is interesting because not all the specifications requirements have specific needs on the microstructures. Otherwise, specific methods are explored by the simulation in [Sections 3.4.3 and 3.4.4](#).

3.4.2 ECR and TCR calibration

Before doing any simulations, the ECR and TCR of the Joule heating model need to be calibrated. The method described in our previous work [22,27] use the temperatures measured on different area of the SPS column to determine the contacts resistances. A simple 8 mm inner diameter configuration ([Fig. 9A](#)) is employed because the geometry of the contact interfaces between the die, punches, and sample are the same compared to the multiple parts configurations ([Figs. 7 and 8](#)). We assume that the ECR and TCR of the one 8 mm sample configuration ([Fig. 9A](#)) are close to the multiple 8 mm samples configurations ([Figs. 7 and 8](#)), at equal temperature and pressure cycle.

The results of the ECR (Ωm^2) and TCR ($\text{m}^2\text{K}/\text{W}$) calibration are reported ([Table 6](#)) for each contact. The measured and modeled temperatures after the calibration are reported in [Fig. 9B](#). Only the electrode/spacer and spacer/spacer contacts are determined from our previous works [65]:

Electrode/spacer:

$$TCR = \frac{1}{1.2 \cdot 10^3} \quad (18)$$

$$ECR = \frac{1}{1.2 \cdot 10^7} \quad (19)$$

Spacer/spacer:

$$TCR = \frac{1}{70 \cdot 10^3} \tag{20}$$

$$ECR = \frac{1}{70 \cdot 10^7} \tag{21}$$

With Tables 4 and 6 the ETMM model parameters are now totally determined.

3.4.3 ETMM simulation for the 37 sample parallel configuration

All the simulations cycles are a 100 K/min temperature ramp up to 1400°C and a 5 min dwell at 1400°C. The pressure is constant during all the cycles and of 25 MPa. In this part of the study, the complete ETMM simulation of the parallel configuration in Fig. 7 is performed. The result of the temperature, relative density, and grain size fields are reported Fig. 12. The select time step for the images (Fig. 12) is 820 s and corresponds to the end of the temperature ramp. This time step is the most interesting because the physics parameters inhomogeneity (temperature, densification, and grain size) are maximum on it (Table 6).

In accordance with the experiment, the ETMM simulation reveals a temperature gradient between the center (hot) and the edge of the die (cool). The temperature difference is roughly 100 K. This thermal gradient has no effect on the sample’s relative density, whose differences are of 2% maximum. However, this thermal gradient causes a radial grain size inhomogeneity, as in Fig. 11.

The interesting point is, even if a thermal gradient appears, no significant differences in relative density are observed. This result can be explained by the intrinsic nature of the parallel configurations, where all the samples

Table 6 Calibrated ECR and TCR

Contact	Type	Values
Spacer/punch	TCR (m ² K/W)	$5 \cdot 10^{-6} + \frac{3 \cdot 10^{-5} \cdot 2000 - T}{T - 50}$
	ECR (Ωm ²)	$\frac{5 \cdot 10^{-9} \cdot 2000 - T}{T - 100}$
Punch/die	TCR (m ² K/W)	$(80 + \frac{50 \cdot 2000 - T}{T - 80}) \cdot 2.4 \cdot 10^{-4}$
	ECR (Ωm ²)	$(-1.33 \cdot 10^{-6} T + 2.5 \cdot 10^{-3}) \cdot 2.8 \cdot 10^{-4}$
Punch/sample	TCR (m ² K/W)	$2.5 \cdot 10^{-5} + \frac{1.5 \cdot 10^{-5} \cdot 2000 - T}{T - 50}$
Sample/die	TCR (m ² K/W)	$(8 \cdot 10^{-6} + \frac{4 \cdot 10^{-6} \cdot 2000 - T}{T - 80}) \cdot 2$

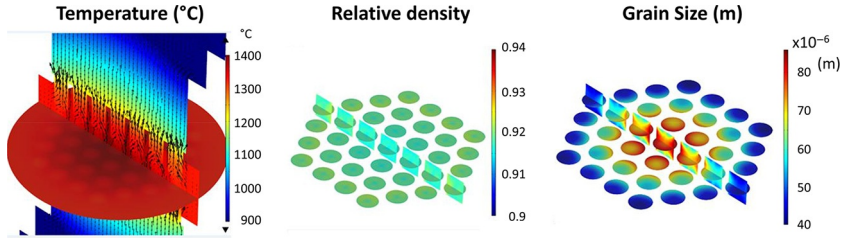


Fig. 12 Multiple parts (37 samples parallel) electro-thermal-mechanical-microstructural simulation at the end of the heating (820 s): on the *left*, the temperature field, in the *middle*, the samples relative density field, and on the *right*, the samples grain size field.

displacements are imposed to be the same. If the center samples are at a hotter temperature, the densification is controlled by the cooler sample at the edge with a slower densification. Then if the temperature and pressure cycle is enough for the densification of the cooler samples, a total densification of all the samples is possible, only a grain size difference appears (Fig. 12).

3.4.4 Corrective simulations for the temperature homogenization of the parallel configuration

If the grain size inhomogeneities observed in both the experiment and the simulation is a problem, it is possible to find solutions for the temperature homogenization responsible for the grain size inhomogeneities. The solutions explored consist to prevent the electric current passage through the center of the die where the temperature is too high. Electric insulations are placed at different areas of the SPS column. Three configurations of electric insulations are studied and reported (Fig. 13) with the corresponding simulated temperature field at 820 s (end of the temperature ramp) and 1200 s (end of cycle).

In corrective configuration 1, two 40 mm diameter insulation disk are placed at 20 mm from the punches, between two graphite foils (Fig. 13). In this configuration, the diminution of the electric current at the center of the die is not sufficient to counter the thermal gradient of the die at 820 s. In corrective configuration 2, the electric insulations are placed directly on the seven punches of the center (Fig. 13). The current deviation is too high in this case and causes a reversal of the temperature gradient with the center of the die cooler than the edge at 820 s. An intermediate solution is to decrease the quantity of punches insulated as in corrective configuration 3 (Fig. 13). In this configuration, the thermal gradient is reduced in all the cycles (820 and 1200 s on the right, Fig. 13). For a parallel configuration, it is

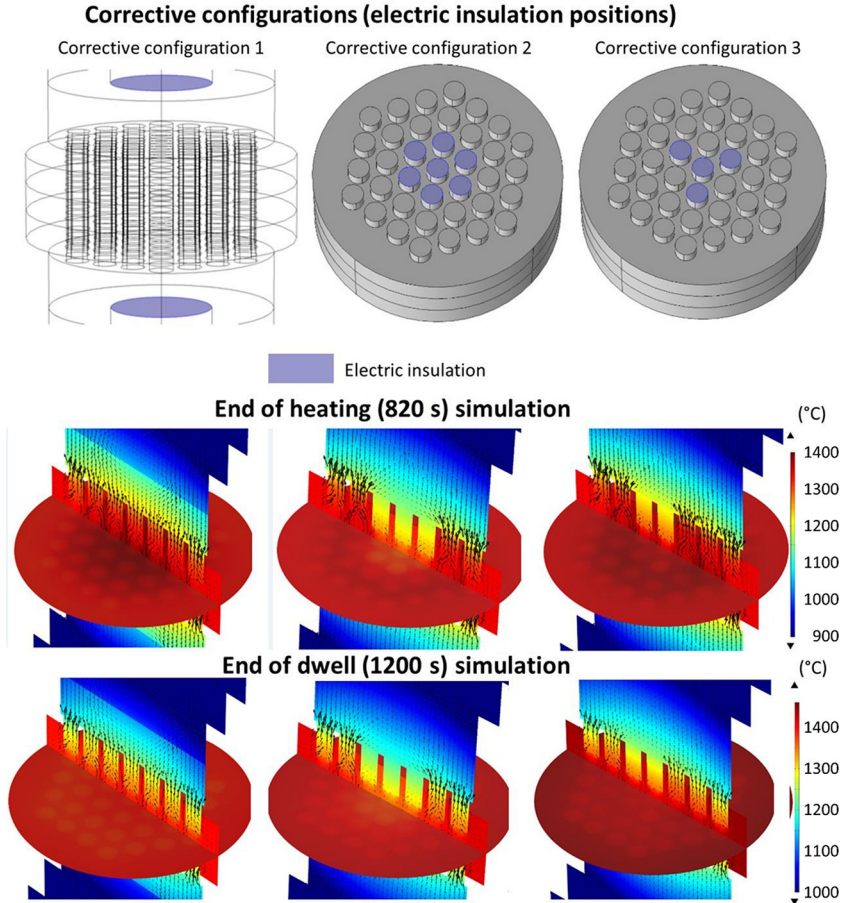


Fig. 13 Corrective configurations for the parallel multiple parts configurations: upper part—positions of different electric insulations (BN spray), lower part—cut plane of the temperature field for the three above configurations at the end of the heating (820 s) and dwell (1200 s).

then possible to homogenize the temperature by a simple placement of electrical insulator on the central punches.

3.4.5 Corrective simulations for the temperature homogenization of the parallel/serial configuration

In order to increase the quantity of simultaneously sintered samples even more, it is necessary to combine the parallel approaches with the series approaches to create parallel/serial configurations, such as those presented in Fig. 8, with three levels and a capacity of 111 samples. Two types of stack are studied: the first case is a simple stacking of the different levels one on the

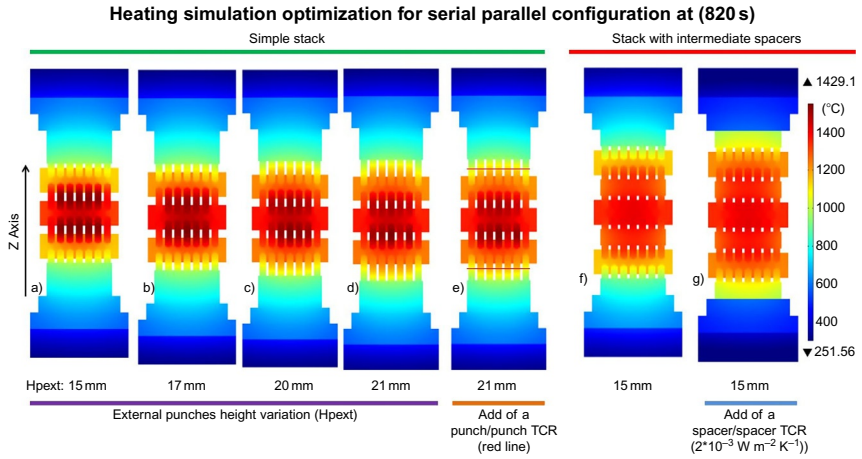


Fig. 14 Optimization simulations of the temperature homogeneity for the serial parallel multiple parts configurations.

other (on the left, Fig. 8), the other is a more classic stacking with intermediate spacers (on the right, Fig. 8). The use of an external die is also studied.

The first parallel serial/simulation, presented in Fig. 14A, show the main difficulty of this type of configuration. A strong thermal gradient appears along the Z-axis with temperature differences of about 200 K. This thermal gradient is the result of a phenomenon of heat accumulation on the central die. The 37 punches of each of the three dies have the same section and the same electric current passing through. The heat generated on the punches of each level is then equal. However, this heat is directly evacuated for the punches in contact with the spacers, compared to those in the middle level. The external punches are then at a cooler temperature. To counter this problem, we must manage to generate a higher quantity of heat in the external punches to compensate the heat lose on the spacers. To do this, we increase gradually the height of the external punches (H_{pext}), as shown in Fig. 14A–D. The sample temperature differences are progressively reduced from 200 K to 100 K, but it is not enough to attain a total homogenization of the temperature. In Fig. 14E, another solution is tested, which consists of a limitation of the quantity of heat evacuated in the spacer by the placement of a high TCR. However, this new solution is not enough to homogenize the temperatures.

The other configuration with intermediate spacer is tested in Fig. 14F and points out the same problem of thermal gradient along the Z-axis. Even the addition of a strong TCR in Fig. 14G does not solve the problem.

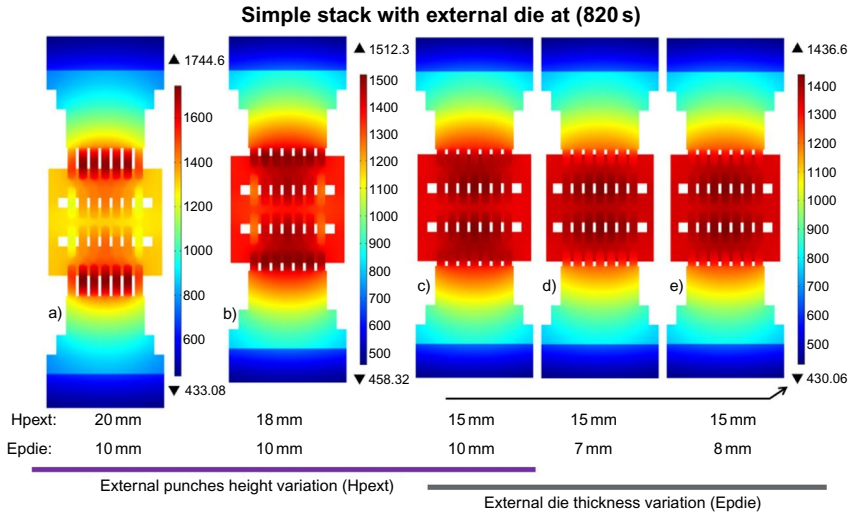


Fig. 15 Optimization simulations of the temperature homogeneity for the serial parallel multiple parts configurations with external die.

The configuration of Fig. 14D is used in Fig. 15A with an external die. This time, a reversal thermal gradient along the Z-axis appears. This new result is more interesting than the others, because the external punches are at a higher temperature. This phenomenon can be explained by the nonequal quantity of current passing through the external and middle level punches. Indeed, the totality of the electric current is forced to pass through the external punches, but in the middle level punches, this quantity of current is divided between the middle level punches and the external die.

Temperature homogenization is now possible because the natural tendency of the parallel/serial configuration is to generate a thermal gradient with cooler external punches, and the external die tends to do the opposite. The homogenization is then performed modifying the external punch height (Fig. 15A–C) first, and the last correction consists of adjusting the external die thickness (Fig. 15C–E).

This new result shows that homogeneous heating is possible for the parallel/serial configuration.

3.5 Conclusions

The multiple parts approaches are an interesting way to increase the productivity of the SPS process. The simple parallel approaches demonstrate the capacity for the simultaneous densification of a high number of samples.

The densification is homogeneous and complete even if a thermal gradient appears between the center and the edge of the die. This phenomenon of auto-stabilization of the relative density is a consequence of the equal imposed displacement on each sample for the parallel configuration. However, even if the thermal gradient is not an obstacle to densification, it creates a small difference in the samples' grain size. Different solutions are tested by the simulations to counter the thermal inhomogeneities for both the parallel and parallel/serial approaches. For the parallel approach, the solution is to place different electric insulations on the central punches. For the parallel/serial configuration, a high degree of thermal gradient appeared along the SPS column. The solution to homogenize the temperatures is to use an external die that allows control of the quantity of current passing through the external and middle punches.

This work shows that obtaining a high quantity of dense samples (111) with homogeneous heating and microstructure is technically possible for the SPS process.

4. Complex shapes

In the vast majority of publications and patents where SPS technique is used for the densification of materials, the parts elaborated have simple planar geometries (i.e., cylindrical or squared shapes, pellets, and/or parts), or none planar but with a homogenous height, in the globality of the part, along the compression direction. The elaboration of complex-shaped specimens with homogeneous density and controlled microstructure is extremely difficult, due to inhomogeneities that can be induced by large temperature and pressure gradients in the specimens. More or less complex-shaped samples have been developed using a strategy of modified design of the punches. For example, E. Olevsky et al., using one or two complex shape punches, have developed complex shaped alumina specimens, but with nonuniform distribution of grain size [66]. Voisin et al. were able to develop a γ -TiAl turbine blade using multiple punches inside the die [67]. Even though the microstructure of the product seems to be homogeneous and the carbide pollution limited to the extreme surface of the part, it seems illusory that parts can be mass-produced with this strategy.

To overcome those situations, Maniere et al. have developed two strategies: (i) a sacrificial material [68] or (ii) the concept of an assembly of porous counter-parts, which define an extended opposite shape of the desired product, covered by a second material acting as a separation interface.



Fig. 16 Complex shapes part elaborated in one single SPS cycle.

The powder of the desired material is thus introduced in the extended cavity defined by the assembly of counter-parts [69,70]. Thus, during the sintering cycle, the part reaches its full density, while the surrounding media compacts not necessarily to full density. After the SPS step, the part can be easily extracted to the surrounding media (densified or not) due to the presence of the separation interface (Fig. 16).

5. Conclusions

Three main conclusions can be drawn from this chapter.

The first one is that the SPS technology has proven to be perfectly repeatable. Pseudo-complex forms, such as “dog bones” made of titanium alloy (Ti-6Al-4V), were densified near to beta transus temperature (T_{β}). The microstructure of this material, evolving very rapidly in the vicinity of T_{β} , is a very good marker of possible thermal gradients seen by the samples. When the tools have been carefully prepared (i.e., the symmetry of the system is respected), perfectly dense ($RD > 99\%$) and reproducible samples have been obtained with mechanical properties comparable to or better than the forged material.

The second point is that the productivity of SPS, a current limit to its industrial development, can be easily increased by densifying in parallel and/or series of materials in multi-samples tools. To do this, it is shown that the finite element modeling of the SPS process is an indispensable tool to better manage the distribution of the current (i.e., temperature) passing through the tools in order to obtain homogeneous samples in density and microstructure, relative to each other.

In the last part of this chapter it is unambiguously shown that the major lock of the SPS concerning the elaboration of complex shapes is now perfectly lifted. Indeed, completely dense materials of complex shapes, such as turbine blades, or very complex, such as compressors, can be obtained with SPS cycles well below 1 h thanks to the patented technology of the mobile interface.

Acknowledgments

A part of the authors thanks D. Poquillon and R. Mainguy for their help on characterizations of the samples and Aubert & Duval for the titanium alloy powder supply; and the other part of the authors, is grateful to the National Research Agency for the financial support. REF ANR: ANR-09-MAPR-0007-MAPR. Impulse.

References

- [1] Z.A. Munir, U. Anselmi-Tamburini, M. Ohyanagi, The effect of electric field and pressure on the synthesis and consolidation of materials: a review of the spark plasma sintering method, *J. Mater. Sci.* 41 (2006) 763–777.
- [2] R. Orrù, R. Licheri, A.M. Locci, A. Cincotti, G. Cao, Consolidation/synthesis of materials by electric current activated/assisted sintering, *Mater. Sci. Eng. R. Rep.* 63 (2009) 127–287.
- [3] S. Grasso, Y. Sakka, G. Maizza, Electric current activated/assisted sintering (ECAS): a review of patents 1906–2008, *Sci. Technol. Adv. Mater.* 10 (2009) 053001.
- [4] O. Guillon, J. Gonzalez-Julian, B. Dargatz, T. Kessel, G. Schierning, J. Räthel, et al., Field-assisted sintering technology/spark plasma sintering: mechanisms, materials, and technology developments, *Adv. Eng. Mater.* 16 (2014) 830–849.
- [5] B.-N. Kim, K. Hiraga, K. Morita, H. Yoshida, Effects of heating rate on microstructure and transparency of spark-plasma-sintered alumina, *J. Eur. Ceram. Soc.* 29 (2009) 323–327.
- [6] G. Lutjering, J. Williams, *Titanium*, Springer, 2007.
- [7] A. Molinari, M. Zadra, Influence of the sintering temperature on microstructure and tensile properties of Ti-6Al-4V produced by spark plasma sintering, in: *Euro PM2009—PM Lightweight & Porous materials I*, 2009, , pp. 4–9.
- [8] L. Bolzoni, I.M. Meléndez, E.M. Ruiz-Navas, E. Gordo, Microstructural evolution and mechanical properties of the Ti-6Al-4V alloy produced by vacuum hot-pressing, *Mater. Sci. Eng. A* 546 (2012) 189–197.
- [9] L. Bolzoni, E.M. Ruiz-Navas, E. Gordo, Flexural properties, thermal conductivity and electrical resistivity of prealloyed and master alloy addition powder metallurgy Ti-6Al-4V, *Mater. Des.* 52 (2013) 888–895.
- [10] K. Zhang, J. Mei, N. Wain, X. Wu, Effect of hot-isostatic-pressing parameters on the microstructure and properties of powder Ti-6Al-4V hot-isostatically-pressed samples, *Metall. Mater. Trans. A Phys. Metall. Mater. Sci.* 41 (2010) 1033–1045.
- [11] K. Crosby, L.L. Shaw, C. Estournes, G. Chevallier, A.W. Fliflet, M.A. Imam, Enhancement in Ti-6Al-4V sintering via nanostructured powder and spark plasma sintering, *Powder Metall.* 57 (2014) 147–154.
- [12] Y. Long, H. Zhang, T. Wang, X. Huang, Y. Li, J. Wu, H. Chen, High-strength Ti-6Al-4V with ultrafine-grained structure fabricated by high energy ball milling and spark plasma sintering, *Mater. Sci. Eng. A* 585 (2013) 408–414.
- [13] F. Zhang, Y. Quan, M. Reich, O. Kessler, E. Burkel, B. Ertuğ (Ed.), *Sintering Applications*, IntechOpen, 2013.
- [14] Y. Kim, E.-P. Kim, Y.-B. Song, S.H. Lee, Y.S. Kwon, Microstructure and mechanical properties of hot isostatically pressed Ti-6Al-4V alloy, *J. Alloys Compd.* 603 (2014) 207–212.
- [15] E.A. Olefsky, L. Froyen, Impact of thermal diffusion on densification during SPS, *J. Am. Ceram. Soc.* 92 (2009) 122–132.
- [16] O. Yanagisawa, H. Kuramoto, K. Matsugi, M. Komatsu, Observation of particle behavior in copper powder compact during pulsed electric discharge, *Mater. Sci. Eng. A* 350 (2003) 184–189.

- [17] M. Otori, Sintering, consolidation, reaction and crystal growth by the spark plasma system (SPS), *Mater. Sci. Eng. A* 287 (2000) 183–188.
- [18] M. Eriksson, Z. Shen, M. Nygren, Fast densification and deformation of titanium powder, *Powder Metall.* 48 (2005) 231–236.
- [19] K. Vanmeensel, A. Laptev, J. Hennicke, J. Vleugels, O. Vanderbiest, Modelling of the temperature distribution during field assisted sintering, *Acta Mater.* 53 (2005) 4379–4388.
- [20] U. Anselmi-Tamburini, J.E. Garay, Z. Munir, Fundamental investigations on the spark plasma sintering/synthesis process I. Effect of dc pulsing on reactivity, *Mater. Sci. Eng. A* 407 (2005) 24–30.
- [21] A. Zavaliangos, J. Zhang, M. Krammer, J.R. Groza, Temperature evolution during field activated sintering, *Mater. Sci. Eng. A* 379 (2004) 218–228.
- [22] C. Arnaud, C. Manière, G. Chevallier, C. Estournès, R. Mainguy, F. Lecouturier, D. Mesguich, A. Weibel, L. Durand, C. Laurent, Dog-bone copper specimens prepared by one-step spark plasma sintering, *J. Mater. Sci.* 50 (2015) 7364–7373.
- [23] Aubert & Duval, Available at <http://www.aubertduval.fr/>.
- [24] S.A. Miller, P.R. Roberts, *ASM Handbook, Vol 7: Powder Metal Technologies and Application*, ASM International, 1998, pp. 97–101.
- [25] U. Kus, J. Huez, G. Chevallier, C. Estournès, D. Delagnes, Relationship between microstructure and tensile properties of a Ti-6Al-4V produced by spark plasma sintering, in: *Proceeding 13th world Conf. Titan*, 2016, , pp. 651–656.
- [26] U. Kus, Etude de la contribution de la technique Spark Plasma Sintering à l'optimisation des propriétés mécaniques de l'alliage de titane TA6V, PhD Thesis, Université Toulouse 3 Paul Sabatier, 2017.
- [27] C. Manière, A. Pavia, L. Durand, G. Chevallier, K. Afanga, C. Estournès, Finite-element modeling of the electro-thermal contacts in the spark plasma sintering process, *J. Eur. Ceram. Soc.* 36 (2016) 741–748.
- [28] C. Manière, L. Durand, E. Brisson, H. Desplats, P. Carré, P. Rogeon, C. Estournès, Contact resistances in spark plasma sintering: from in-situ and ex-situ determinations to an extended model for the scale up of the process, *J. Eur. Ceram. Soc.* 34 (2017) 1593–1605.
- [29] K. Mutombo, P. Rossouw, G. Govender, Mechanical properties of mill-annealed Ti-6Al-4V investment cast, *Mater. Sci. Forum* 690 (2011) 69–72.
- [30] G. Abouelmagd, H.P. Buchkremer, E. El-Magd, D. Stover, Mechanical properties of a Ti-6Al-4V alloy processed by powder metallurgy, *J. Mater. Process. Technol.* 37 (1993) 583–597.
- [31] M.J. Donachie, *Titanium, a Technical Guide*, ASM International, 2000.
- [32] R.R. Boyer, G. Welsch, E.W. Collings, *Materials properties Handbook—Titanium Alloys*, ASM International, 1994.
- [33] *ASM Handbook, Properties and Selection: Nonferrous and Special-Purpose Materials*, vol. 2, ASM International, 1995.
- [34] A. Bonhomme, Développement et application industrielle du frittage flash de poudres métalliques, in: *Oral Conference, MATERIAUX2014*, 2014.
- [35] M. Cologna, B. Rashkova, R. Raj, Flash Sintering of Nanograin Zirconia in <5 s at 850°C, *J. Am. Ceram. Soc.* 93 (2010) 3556–3559.
- [36] E. Olevsky, Ultra-rapid field-assisted consolidation of powders, in: *Oral conference, 3rd International Workshop on Spark Plasma Sintering*, Capbreton France, 2014.
- [37] M. Tokita, Method and System for Automatic Electrical Sintering, US Patent No. 6,383,446 (2002).
- [38] M. Tokita, K. Nakagawa, Rotary Table Type Electric Heating Pressure Sintering Apparatus, JP Patent No. JP2002206102 (2002).
- [39] http://www.fct-systeme.de/fr/content/Spark_Plasma_Sintertechnologie/, 2016.

- [40] K.J. Micklash, M.S. Bailey, Hot Pressing Apparatus and Method for Same, US Patent No. US 2013/0140740 A1(2013).
- [41] J. Schmidt, A. Knote, M. Armbrüster, T. Weißgärber, B. Kieback, Spark Plasma Sintering of Diamond Impregnated Wire Saw Beads, in: PM2010 World Congress—Diamond Tools, 2010.
- [42] A.V. Smirnov, D.I. Yushin, I.A. Zverev, A.R. Maslov, R. Torrecillas, Modeling of hybrid method as combined spark plasma sintering and hot pressing physical processes, *Mec. Ind.* 16 (2015) 712.
- [43] K. Vanmeensel, A. Laptev, O. Van der Biest, J. Vleugels, Field assisted sintering of electro-conductive ZrO₂-based composites, *J. Eur. Ceram. Soc.* 27 (2007) 979–985.
- [44] K. Matsugi, H. Kuramoto, T. Hatayama, O. Yanagisawa, Temperature distribution at steady state under constant current discharge in spark sintering process of Ti and Al₂O₃ powders, *J. Mater. Process. Technol.* 134 (2003) 225–232.
- [45] G. Molénat, L. Durand, J. Galy, A. Couret, Temperature control in spark plasma sintering: an FEM approach, *J. Metall.* 2010 (2010) 1–9.
- [46] J.B. Allen, C. Walter, Numerical simulation of the temperature and stress field evolution applied to the field assisted sintering technique, *ISRN Mater. Sci.* 2012 (2012) 1–9.
- [47] U. Anselmi-Tamburini, S. Gennari, J.E. Garay, Z.A. Munir, Fundamental investigations on the spark plasma sintering/synthesis process, *Mater. Sci. Eng. A* 394 (2005) 139–148.
- [48] A.I. Raichenko, E.S. Chernikova, A mathematical model of electric heating of the porous medium using current-supplying electrode/punches, *Powder Metall. Met. Ceram.* 38 (1989) 265–371.
- [49] M. Yoneyal, T. Ikeshoji, et al., *Mater. Trans.* 42 (2001) 2165–2171.
- [50] A. Pavia, L. Durand, F. Ajustron, V. Bley, G. Chevallier, A. Peigney, et al., Electro-thermal measurements and finite element method simulations of a spark plasma sintering device, *J. Mater. Process. Technol.* 213 (2013) 1327–1336.
- [51] G. Maizza, S. Grasso, Y. Sakka, Pressure effects on temperature distribution during spark plasma sintering with graphite sample, *J. Mater. Sci.* 44 (2009) 1219–1236.
- [52] S. Grasso, Y. Sakka, G. Maizza, Pressure effects on temperature distribution during spark plasma sintering with graphite sample, *Mater. Trans.* 50 (2009) 2111–2114.
- [53] C. Manière, A. Pavia, L. Durand, G. Chevallier, V. Bley, K. Afanga, et al., Pulse analysis and electric contact measurements in spark plasma sintering, *Electr. Power Syst. Res.* 127 (2015) 307–313.
- [54] X. Wei, D. Giuntini, A.L. Maximenko, C.D. Haines, E.A. Olevsky, Experimental investigation of electric contact resistance in spark plasma sintering tooling setup, *J. Am. Ceram. Soc.* 98 (2015) 3553–3560.
- [55] G. Maizza, S. Grasso, Y. Sakka, Moving finite-element mesh model for aiding spark plasma sintering in current control mode of pure ultrafine WC powder. *J. Mater. Sci.* 44 (2009) 1219–1236, <https://doi.org/10.1007/s10853-008-3179-8>.
- [56] E.A. Olevsky, Theory of sintering: from discrete to continuum, *Mater. Sci. Eng. R. Rep.* 23 (1998) 41–100.
- [57] E.A. Olevsky, C. Garcia-Cardona, W.L. Bradbury, C.D. Haines, D.G. Martin, D. Kapoor, Fundamental aspects of spark plasma sintering: II. Finite element analysis of scalability, *J. Am. Ceram. Soc.* 95 (2012) 2414–2422.
- [58] C. Manière, L. Durand, A. Weibel, C. Estournès, Spark-plasma-sintering and finite element method: From the identification of the sintering parameters of a submicronic α -alumina powder to the development of complex shapes, *Acta Mater.* 102 (2016) 169–175.
- [59] C. Manière, L. Durand, A. Weibel, C. Estournès, A predictive model to reflect the final stage of spark plasma sintering of submicronic α -alumina, *Ceram. Int.* 42 (2016) 9274–9277.

- [60] C. Manière, L. Durand, C. Estournès, Powder/die friction in the spark plasma sintering process: modelling and experimental identification, *Scr. Mater.* 116 (2016) 139–142.
- [61] https://www.mersen.com/uploads/tx_mersen/15-speciality-graphite-materials-for-sintering-Mersen_10.pdf, 2016.
- [62] https://www.mersen.com/uploads/tx_mersen/12-PAPYEX-graphite-expanse-Mersen.pdf, 2016.
- [63] <http://www.mersen.com/en/products/advanced-materials-and-solutions-for-high-temperature/high-temperature-thermal-insulation.html>, 2016.
- [64] M.I. Mendelson, Average Grain Size in Polycrystalline Ceramics, *J. Am. Ceram. Soc.* 52 (1969) 443–446.
- [65] C. Manière, Spark Plasma Sintering: Modeling, Device and Materials Approaches, PhD Thesis. 2015, Université Toulouse 3 Paul Sabatier.
- [66] E. Olevsky, E. Khaleghi, C. Garcia, W. Bradbury, Fundamentals of spark plasma sintering: applications to net-shaping of high strength temperature resistant components, *Mater. Sci. Forum* 654 (2010) 412–415.
- [67] T. Voisin, J.P. Monchoux, L. Durand, N. Karnatak, M. Thomas, A. Couret, An innovative way to produce γ -TiAl blades: spark plasma sintering, *Adv. Eng. Mater.* 17 (10) (2015) 1408–1413.
- [68] C. Manière, L. Durand, A. Weibel, G. Chevallier, C. Estournès, A sacrificial material approach for spark plasma sintering of complex shapes, *Scr. Mater.* 124 (2016) 126–128.
- [69] C. Manière, E. Nigito, L. Durand, A. Weibel, Y. Beynet, C. Estournès, Spark plasma sintering and complex shapes: the deformed interfaces approach, *Powder Technol.* 320 (2017) 340–345.
- [70] C. Estournès, C. Manière, L. Durand, French Patent FR20150060564 20151104; WO2016EP76657 20161104 (n.d.).